Design of a Universal Inductive Charger for Multiple Electric Vehicle Models

Nan Liu, *Student Member, IEEE*, and Thomas G. Habetler, *Fellow, IEEE*

***Abstract*—Inductive power transfer technology has become a popular solution for battery charging of electric vehicles (EVs). However, problems such as varied magnetic coupling caused by coil misalignment still limit its practical applications, by safety and stability issues. Meanwhile, the growing market of EVs asks for a universal charger for various models. This paper presents the design process of a universal inductive charger (UIC) for EVs. The proposed UIC is capable of adaptively providing a constant or controllable charging voltage to various EVs, with a wide range of varied magnetic coupling between the transmitting and receiving coils. With a series-connected *LC* circuit, zero-voltage switching of the primary dc–ac inverter is universally realized in every charging cycle. A simple yet effective control method based on the frequency variation is used to automatically select the optimal frequency in different coupling conditions and adjust the frequency during the charging process. The design of the charging interface is also optimized with higher efficiency and power-transfer capability. Simulations and prototypes validate that the proposed UIC is accurate, robust, and applicable.**

***Index Terms*—Frequency control, inductive charging interface, universal inductive charger (UIC), zero-voltage switching (ZVS).**

I. Introduction

INDUCTIVE power transfer (IPT), also known as inductive charging, is used to inductively transfer the high-frequency ac power in the transmitting coil to the receiving coil in the load by loosely coupling [1]–[3]. The IPT is a promising method for charging electrical vehicles (EV), in a convenient, safe, and aesthetic way. However, problems such as coil misalignment and varied charging distance (air gap) change the magnetic coupling between the transmitting and receiving coils and lead to different electrical characteristics for each charging cycle. An adaptive control method dealing with a wide range of mutual coupling is necessary for the practical application of IPT. Moreover, as various EV models have already existed on market and more will be produced in the future, it is meaningful to design a universal charger, which is suitable for charging EVs of different designs, especially with various receiving coils. As a result, the goal of this paper is to design a universal inductive charger (UIC) (stationary, Level 1 and 2 charging), which could provide: 1) a constant or controllable charging voltage to the load even with a wide range of varied magnetic coupling; 2) adaptive charging to the EVs with various design of receiving coils and resonant circuits; 3) high efficiency during each charging process; and 4) automatic and simpler control, without wireless communications.

Most of the current IPT research concentrates on three aspects: the topologies of resonant circuits, the control method for the inverters or converters in the charger or load, and the design of the charging interface. Since this paper only focuses on the charger (also defined as the primary-side system) design, the charger itself is mainly analyzed.

Two common topologies for the primary resonant circuit, the series- (S-) and parallel-connected (P-connected) *LC* circuits, have been tested in previous work for different applications [4]–[10]. For basic analysis, an S-connected *LC* circuit is easier to tune and performs better in harmonics reduction; while a P-connected *LC* circuit acts as a current source and has a low voltage stress on the resonant capacitance. Some papers select *S*- or P-connected *LC* circuit according to more specific issues, such as the efficiency [6], [11]–[13]. More developed topologies have also been proposed [14], [15]. For example, the system proposed in [15] applies a typical topology, the *LCC* circuit (T-*LCL*). The *LCC* circuit combines the advantages of S- and P-connected resonant circuits. The zero-current switching (ZCS) can be realized through the charging process, while the output current is a constant independent of load, making it ideal for the battery charging. However, more loss is generated by parasitic elements in resonant components of *LCC*. Considering the soft switching of the full-bridge inverter of the charger, the ZCS is not efficient when the inverter is built by MOSFETs with high frequency ac power and a high input voltage. Moreover, the constant-current mode is not necessary for the Level 1 and 2 charger, because EVs have their own on-board ac–dc converters to control the charging current and voltage. So the output of the *LC* resonant circuit on the EV is connected to the on-board converter directly, which prefers a stable voltage input. So a constant-voltage mode is more suitable for inductive charging. To select the resonant circuit in the UIC, it also needs to consider a much wider range of mutual inductance caused by varied coil misalignment or air gap in different charging cycles. The UIC should be kept as a constant-voltage source with varied magnetic coupling.

For the control method, the relevant research emphasizes on modulation of the inverter in front of the primary resonant circuit. The pulse-width modulation (PWM) is most commonly used as the basic modulation. For example, a typical voltage control method developed in [16] realizes constant charging voltage with ZVS operation by a fixed frequency in resonant

Manuscript received October 1, 2014; revised December 14, 2014; accepted January 14, 2015. Date of publication January 26, 2015; date of current version July 10, 2015. Recommended for publication by Associate Editor G. A. Covic.

The authors are with the School of Electrical and Computer Engineering, Georgia Institute of Technology, Atlanta, GA 30318 USA (e-mail: nliu37@gatech.edu; thabetler@ece.gatech.edu).

Color versions of one or more of the figures in this paper are available online at http://ieeexplore.ieee.org.

Digital Object Identifier 10.1109/TPEL.2015.2394734

circuits. However, the relevant systems do not own adaptability over coupling variances, because they need the varied magnetic coupling to be limited in a certain range, and the preset "optimal" ac frequency is still not always the best in hypothetical conditions. Moreover, the signal sensing on the voltage and current is difficult when the frequency is very high (>80 kHz). The speed of sensing and data calculations limits the practical application of the PWM. The frequency-control scheme has also been applied by some previous papers [17]–[19]. But, most of the proposed variable-frequency methods depend on wireless communications between the charger and the load. Besides increasing costs, wireless devices can hardly transmit the transient information of high-frequency V&I. Some previous work applied auxiliary components to get the information for frequency control [18]–[20]. For instance, the inductive charger developed in [18] is able to seek for the optimal frequency before the charging process. However, the control method needs complicated calculations based on an additional "dummy resistor" in the load side, leading to more complex design and modulation of the charger, lower efficiency, and higher cost. In fact, a low-cost, adaptive, and efficient scheme for frequency control has never been proposed. For the specific values of the ac frequency, they are also different in previous works. The resonant frequency [1], [21], [22], the unity-gain frequency [18], the frequency between them [16], and even multiple frequencies [23], have been applied in various works. As a result, the UIC needs a more adaptive and simpler control method to seek for a reasonable ac frequency in various charging situations (wider range of mutual inductance).

For the charging interface, there are two basic structures: coils with transformer cores (E- or U-core) and coils with plane core. The plane-core structure (also known as "pad") is more popular nowadays, with more aesthetic appearance and larger tolerance on horizontal misalignment [1], [3], [21], [22], [24]–[26]. Two types of pads: the nonpolarized pad design made of a single coil (square-shaped and circular pad, etc.) and the polarized pad design made of multiple coils (bipolar pad, DDP, etc.) are the most commonly used ones. A nonpolarized pad generates perpendicular magnetic field while a polarized pad provides parallel field pattern. For a nonpolarized pad, it has the same tolerance of misalignment in each direction and is much easier to operate. The polarized pads have been proved to be better than the nonpolarized pads, for higher tolerance to the horizontal misalignment [21], [22], [27]. But the higher coupling of polarized pads only exists in the lateral direction. And, this is not the absolute advantage of the polarized pads, because the tolerance to horizontal misalignment and air gap can be improved by enlarging the size of charging coils [3], [28]. Moreover, magnetic simulations show that the performance of a polarized pad is influenced with the mistaken coupling caused by coil misalignment, as the flux in one coil of the receiving pad couples with the wrong coil of the transmitting pad, when they are partly faced to each other [3]. For the shape of the coils, square-shaped ones are better in magnetic coupling and transmitting efficiency than circular ones.

Different from the previous works, an UIC is proposed in this paper to provide stable and high-efficiency charging to different EV models even with the influence of various receiving coils and varied magnetic coupling. This paper is organized as follows. Section II compares different resonant circuits with each other and selects the S-connected *LC* as the optimal topology, which provides a constant charging voltage to the load and maintains higher efficiency during the whole charging process. Section III proposes an effective and universal control method to select the optimal ac frequency and adjust the frequency during the charging process; wireless communication is not necessary. Section IV analyzes different structures of the charging pads and demonstrates that the square-shaped pad with perpendicular flux has better coupling effect and higher efficiency when the overall size is limited in practical applications. In Section V, experiment results by a prototype are used to test the applicability of the proposed UIC design. Finally, Section VI summarizes the contributions.

II. Resonant Circuit of the UIC

By circuit analysis, the only connection between the primary side (the charger) and the secondary side (the charged EV) is the mutual inductance between the primary and secondary inductances. However, the mutual inductance is varied by the air gap and horizontal misalignment between the transmitting and receiving coils. For an UIC, the first challenge is to provide stable and controllable power to the load through the two *LC* resonant circuits, even with a wide range of varied mutual inductance. Another challenge for an UIC is from the different design characteristics in different models of EVs, including coils (inductances), resonant capacitances, and so on. An UIC should be capable of adapting to the variances of the secondary circuits in various EVs. As a result, an optimal connection of the primary *LC* circuit should be selected, to make it possible that the loads could get a constant voltage during each charging cycle, even the mutual inductance is various in different charging cycles, or the secondary *LC* circuits in the loads are S- or P-connected, or with various values of the secondary inductance.

A. S- or P-Connected LC

In a typical IPT system, there are four common combinations of resonant circuits: the series–series connected (SS-connected), series-parallel connected (SP), parallel–parallel connected (PP), and parallel–series connected (PS) *LC*s, as shown in Fig. 1. The characteristics of S- and P-connected *LC* circuits have been analyzed in [4] and [29]. The resonant frequency is commonly chosen as the optimal ac frequency in the resonant circuit by the equation

$$\omega_0 = 2\pi f_0 = 1/\sqrt{L_i C_i} \quad i = 1, 2. \tag{1}$$

In practical applications, the charger with a P-connected *LC* has some disadvantages, such as the high turn-off current, or the nonzero load reactance, which reduce the efficiency and influence the tuning of the *LC* circuits [3], [4], [29]. The S-connected circuit is preferred, for its easy tuning in long-track applications, relatively fixed value of resonant capacitance with various mutual inductances, and good harmonics reduction in loosely

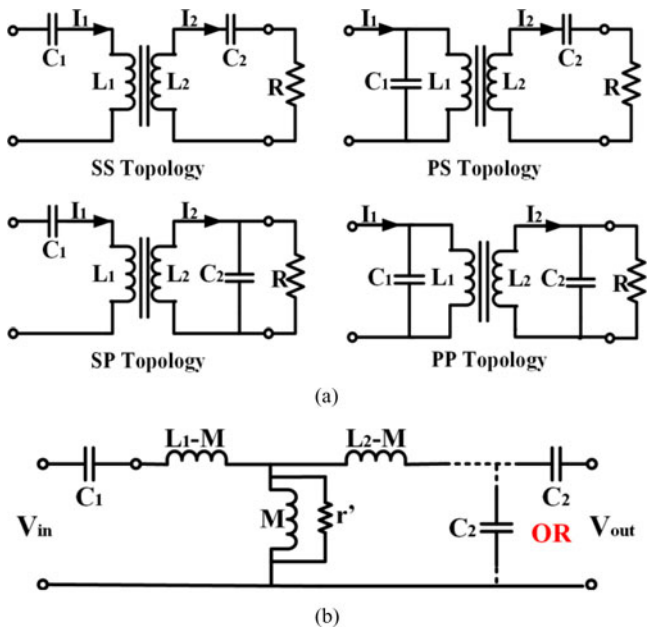

Fig. 1. (a) Four basic topologies of the *LC* resonant circuits in an IPT system; and (b) equivalent circuit when the primary *LC* circuit is S-connected, where L_1 and C_1 are the primary inductance and capacitance, L_2 and C_2 are the secondary inductance and capacitance, *M* is the mutual inductance between L_1 and L_2, *R* is the equivalent resistance of the load, and *r'* is an equivalent resistor simulating the power loss caused by flux leakage and unwanted coupling.

coupling conditions [4], [5]. Moreover, adaptive control is also an essential requirement to realize universal charging. The parallel tuning in the primary *LC* circuit is dependent on both the magnetic coupling and the load. But For the S-connected *LC* circuit works as a constant-voltage source in every single charging cycle, without influence from the load. In practical applications, EVs have on-board ac–dc converters to control the charging current and voltage in the typical Level 1 and 2 charging [30], and the common on-board converters prefer a constant voltage input. As a result, a constant-voltage source is a better equivalent model for the combination of the primary and secondary *LC* circuits.

The circuit analysis of the IPT system is based on a mutual-inductance coupling model shown in Fig. 1(b). The dc characteristics of the resonant circuits, including the voltage gain and the equivalent load-phase angle versus the ac frequency, can be calculated. The voltage gain is

$$G = |V_{\text{out}}/V_{\text{in}}| \tag{2}$$

where V_{in} is the input voltage of the primary *LC* circuit and V_{out} is the output voltage of the secondary *LC* circuit. The equivalent load-phase angle is the phase angle of the equivalent impedance looking from the input of the primary *LC* circuit. In the SS topology, the equivalent impedance is

$$Z_{\text{total}} = 1/(j\omega C_1) + j\omega L_1 + \omega^2 M^2/(j\omega L_2 + 1/(j\omega C_2) + R) \tag{3}$$

in the SP topology, the equivalent impedance is

$$Z_{\text{total}} = 1/(j\omega C_1) + j\omega L_1 + \omega^2 M^2/(j\omega L_2 + (1/(j\omega C_2))||R). \tag{4}$$

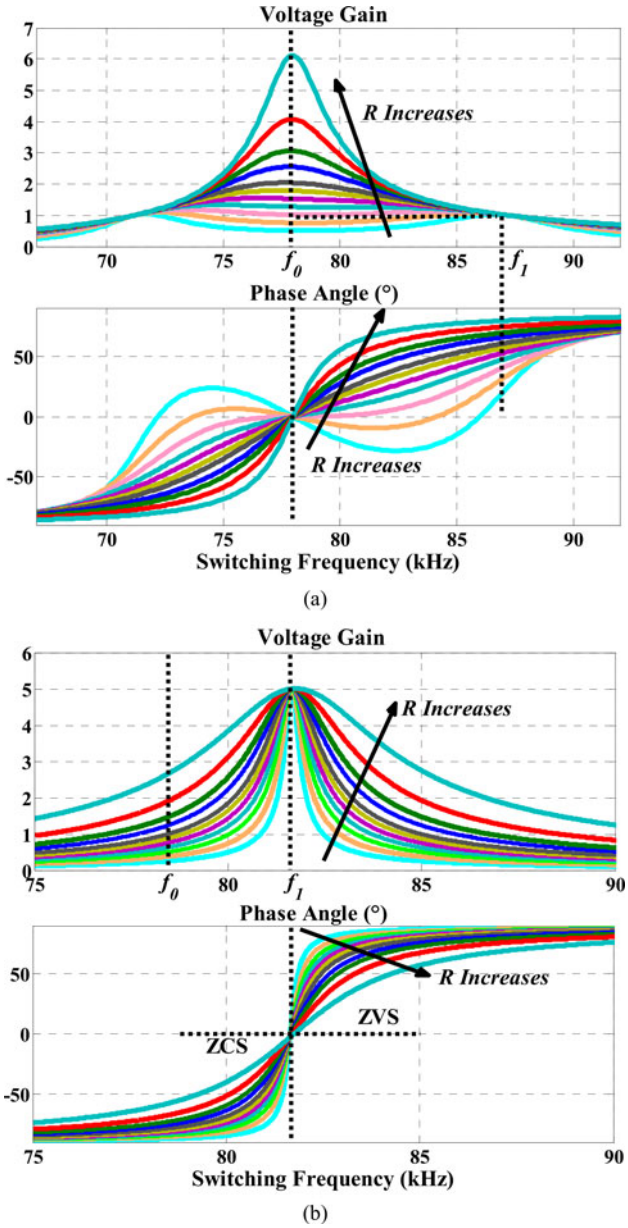

Fig. 2. Simulated dc characteristics: the voltage gain and load-phase angle versus the ac frequency in (a) SS-connected *LC* and (b) SP-connected *LC*, where $L_1 = 199.5\ \mu$H and $L_2 = 200.8\ \mu$H, $C_1 = 20.87$ nF and $C_2 = 20.73$ nF (the resonant frequency $f_0 = 78$ kHz), $M = 40\ \mu$H, and $R = 10$, 15, 20, 25, 30, 35, 40, 50, 60, 80, 120 Ω.

When the load contains an S-connected *LC* circuit, the simulated dc characteristics (by Simulink) of the SS topology in a single charging cycle is shown in Fig. 2(a). The following conclusions can be drawn:

1) The voltage gain is not fixed at the resonant frequency f_0 in various load conditions and can be extremely high with a light load (*R* is very large).
2) When *M* is fixed, each curve of the voltage gain in a varied load condition (*R* varies) goes through a fixed-gain point (the unity-gain point when $L_1 = L_2$) at the frequency f_1. The Z_{total} is inductive beyond f_1 (the input voltage leads the input current), leading to the ZVS operation (turn ON)

of the primary dc–ac inverter. The existence of the fixed-gain point is not influenced by "bifurcation." Although Z_{total} is kept purely resistive at the resonant frequency f_0, the system with the frequency f_1 provides a much more stable output voltage: a constant voltage gain not influenced by varied load resistance. This also means that the transferred real power is not influenced by mutual inductance *M*, when the ac frequency is f_1, according to $P = V^2/R$.

3) The voltage gain at the fixed-gain point is determined by the values of the primary and secondary inductances, as

$$G = \sqrt{L_2/L_1}. \tag{5}$$

4) The frequency at the fixed-gain point f_1 is influenced by the mutual inductance, and can be calculated by

$$f_1 = \sqrt{\frac{\sqrt{L_2}}{C_1(L_1\sqrt{L_2} - M\sqrt{L_1})}}/2\pi. \tag{6}$$

5) From the condition that *R* becomes $+\infty$ and the voltage gain still passes through the fixed-gain point

$$G = \sqrt{\frac{L_2}{L_1}} = \frac{j\omega_1 M}{j\omega_1 M + j\omega_1(L_1 - M) + \frac{1}{j\omega_1 C_1}}. \tag{7}$$

6) For each curve of the load-phase angle with a heavy or medium load, there is only one zero-crossing point between the resonant frequency and the fixed-gain point.

So if the frequency is set to be f_1, the primary inverter will keep working with ZVS during the whole charging process. The voltage gain *G* will be kept constant during the charging process, which is much easier for the on-board ac–dc converter to regulate the charging voltage, current, and power. The value of f_1 can be acquired by measuring the zero-crossing point of the load-phase angle versus frequency, which is higher than the resonant frequency f_0. Note that the analysis is based on the assumption that the resonant frequencies determined by the *L*s and *C*s of the primary and secondary resonant circuits, are the same or close to each other. It is reasonable for EV manufacturers to set the secondary *LC* circuits with the same resonant frequency, as the charger. EV manufacturers can select an appropriate value of the self-inductance of the receiving coil first, and choose *C* accordingly, by (1). As there has already been a standard (SAE J2954) limiting the ac frequency used in wireless charging of EVs (81.38 $\sim$ 90 kHz), each EV is proposed to work with the ac frequency in a specific range. The standard also requires the proximity of the resonant circuits on EVs to the primary resonant circuit of the charger, in the frequency settings. Also note that the preset resonant frequencies of the charger and EVs are not necessary to be in the standard range, but their working frequency is. As a result, the assumptions for the simulations in Fig. 2 are reasonable: similar resonant frequency of the *LC* circuits on both sides and the working frequency limited in the standard range. As the voltage gain at f_1 is determined by the self-inductances of the transmitting and receiving coils, the EV manufacturers should set the value of L_2 according to the specific voltage requirements of their EVs.

When the load contains a P-connected *LC* circuit, the simulated dc characteristics of the SP topology are shown in Fig. 2(b). Similar to the SS-connected *LC* circuits, there also exists a fixed-gain point at the frequency f_1. All of the voltage-gain curves pass through the fixed-gain point at f_1, no matter what the value of *R* is. With the same method used in the SS topology, the voltage gain at the fixed-gain point can be calculated by

$$G = L_2/M. \tag{8}$$

The value of f_1 is also determined by the mutual inductance *M*, as

$$f_1 = \sqrt{\frac{L_1}{C_2(L_1L_2 - M^2)}}/2\pi. \tag{9}$$

However, if the frequency is set to be f_1, Z_{total} will be capacitive during the whole charging process, because the load-phase angle is slightly lower than 0. In fact, the zero-crossing point of each load-phase-angle curve is very close to f_1. If the frequency is set to be slightly higher than f_1, ZVS can be realized. From the curves of the voltage gain, the voltage gain is very sensitive to the frequency variance (a P-connected *LC* can be treated as a current source). Because of the limitation on the voltage gain, the frequency must be carefully controlled.

Hence, compared with P-connected *LC* circuit, the S-connected *LC* circuit is much more suitable for universal charging. The S-connected *LC* circuit is capable of charging different types of EVs with higher efficiency, stable output voltage and easier operations, for the following four reasons:

1) For the primary inverter with an S-connected *LC* circuit, the voltage gain *G* at the fixed-gain point is kept constant during the charging process, which is an ideal input for the on-board ac–dc converter.
2) For the primary inverter with an S-connected *LC* circuit, if the frequency is set as the fixed-gain point f_1, ZVS is kept during the charging process.
3) The fixed-gain point always exists, if the resonant frequencies determined by *LC*s of the charger and the EV are equal or nearly equal. It means that the optimal frequency is fixed during a specific charging cycle and can be found by detecting the load-phase angle, although the frequency f_1 is varied by the mutual inductance. This also makes it possible to control the inductive charger without wireless communications between the two sides.
4) For each curve of the load-phase angle in Fig. 2, there is only one zero-crossing point beyond f_0. This means that the fixed-gain point can be easily acquired by seeking from f_0 to higher values until the load-phase angle becomes 0.

B. S-Connected LC or LCC

Another popular topology applied in inductive charging is the *LCC* resonant circuit, as shown in Fig. 3. Combining good characteristics of S- and P-connected *LC* circuits, an *LCC* circuit has a constant output current independent of load and a narrow switching frequency range [2], [15], [31]. But an *LCC* circuit has to work in the ZCS mode to acquire the ideal output, because the ZVS can only be realized at the negative slope of the curve of the

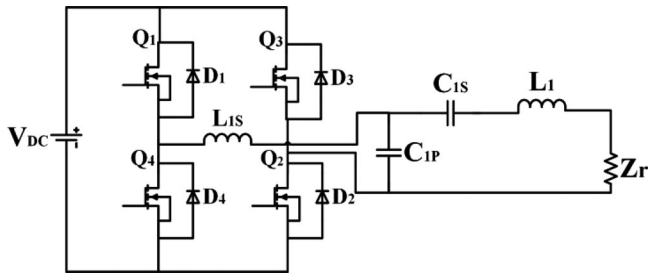

Fig. 3. Simplified model of the inductive charger with *LCC* resonant circuit, where L_{1s} is the added S-connected inductor, C_{1p} is the added parallel connected capacitor, the C_{1s} is the resonant capacitor with L_1, and Z_r is reflected impedance from the secondary side to the primary side.

voltage gain versus the frequency, leading to an unreasonably large range of the optimal frequency from a heavy to light load. However, in a high-frequency inverter using MOSFETs, the ZVS (ZVS turn ON) mode is more efficient and safer than ZCS, especially with a high input voltage, because of lower turn-on losses and avoiding high current stress. Moreover, for universal applications, system may adjust the frequency to acquire the voltage gain in a typical range, like 0.5∼2. In this condition, an S-connected *LC* circuit only needs to vary the frequency in a significantly smaller scope than the *LCC* or the P-compensated *LC* circuits. In another respect, more resonant components used in the *LCC* circuit lead to more energy stored in the inductors and capacitors. This generates more power loss by parasitic elements in the resonant components. As a summary, the *LCC* circuit can rarely realize the stable output and a higher efficiency in ZVS mode at the same time.

C. Existing Problems With S-Connected LC

For an UIC with an S-connected *LC* circuit, there are some problems to be solved before realizing "real" universality. An obvious problem is the high percentage of reactive power in a light load, when the load contains an S-compensated *LC* circuit and the frequency is set to be f_1. High percentage of reactive power means significant power loss; meanwhile, more stress of the power-factor-correction is put on the dc converter in front of the primary dc–ac inverter. Accordingly, the UIC could adjust the frequency to a lower value to reduce the reactive power. Note that the reduction cannot be too large since a limitation on the ac frequency.

Another problem is about the detection of f_1. Because the variance of the ac frequency has an obvious influence on the output voltage and the load-phase angle, a small shift of the frequency generates an unwanted change of the output. Therefore, an accurate control method or loop is necessary for tracking f_1. An effective algorithm to distinguish the connection of *LC* in the secondary resonant circuit is also helpful.

III. Control-Loop Design

There is an ac source generating the high-frequency ac (normally in the range of 20 ∼ 200 kHz in most of the current research) to the primary *LC* resonant circuit. The main function of the ac source includes: converting the ac from the grid to a stable dc output while doing PFC, and then, generating a high-frequency ac to the following *LC* circuit by the designed control methods, summarized as the ac–dc–ac conversion. This paper concentrates on the control of the primary ac power source and the coordination between the charger and the load. The ac source in an inductive charger is a typical full-bridge dc–ac inverter, which is normally controlled by sinusoidal pulse-width modulation (SPWM), which is used to modulate the duty cycle of the switching signal, with a fixed frequency. However, the SPWM is not the focus here, but can be treated as the inner loop of the dual-loop control model. In fact, with the ac frequency higher than 80 kHz, the V&I sensing on the *LC* circuits is difficult, because of the speed limitation of sensors or analog-to-digital converters (ADC). This strongly limits PWM application in modulating the resonant circuits. Therefore, the variable-frequency control would be preferred. The PWM (with PFC) can be operated in the ac–dc converters on the primary side to regulate the input voltage, or on the secondary side to control the charging current. As a result, the default duty cycle is set to be 50% in this paper.

The main focus of this section is the frequency control for universal charging. The UIC is proposed to select the optimal frequency automatically before the charging process, and adjust the frequency during the charging process, if needed. According to the previous analysis, the frequency at the fixed-gain point f_1 is chosen as the optimal ac frequency.

A. Control Process

A few methods have been proposed on searching for f_1. For example, a typical method proposed in [18] searches from a preset higher frequency f_2 to the resonant frequency f_0 to acquire f_1. However, all of these methods need additional components and wireless-communication devices [18], [32], [33].

For universal charging, a simpler and faster method of searching f_1 is proposed here, as shown in Fig. 4. The method is based on the curves of the load-phase angle shown in Fig. 2. At the beginning of charging, the ac–dc rectifier in the UIC provides a low input dc voltage $V_{\rm start}$ to the dc–ac inverter (lower than the full-input voltage). The UIC adjusts the ac frequency from f_0 to higher values step by step (increasing step $= \Delta f$) while measuring the load-phase angle θ between the input voltage and current. According to the load-phase angle curves shown in Fig. 2, the fixed-gain point (f_1) can be acquired when the angle θ is above zero. At last, the UIC sets the ac frequency to be f_1 and increases the input dc voltage to the value $V_{\rm in}$, which is the input voltage for the full power level. Then, the output voltage of the secondary *LC* circuit (or the input voltage of the on-board ac–dc converter) is maintained constant during the whole charging process, according to the specific ratio of $V_{\rm out}$ to $V_{\rm in}$ at the fixed-gain point. In practical operation, the variance of the ac frequency during the charging process influences the power distribution on *LC* circuit and the power flow between the two sides. Unreasonably fast variance of the frequency generates instability and power emissions in high-power applications. So

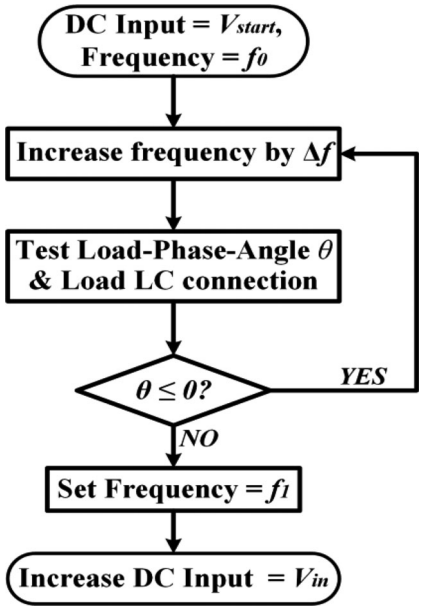

Fig. 4. Flowchart of the proposed control method for tracking f_1.

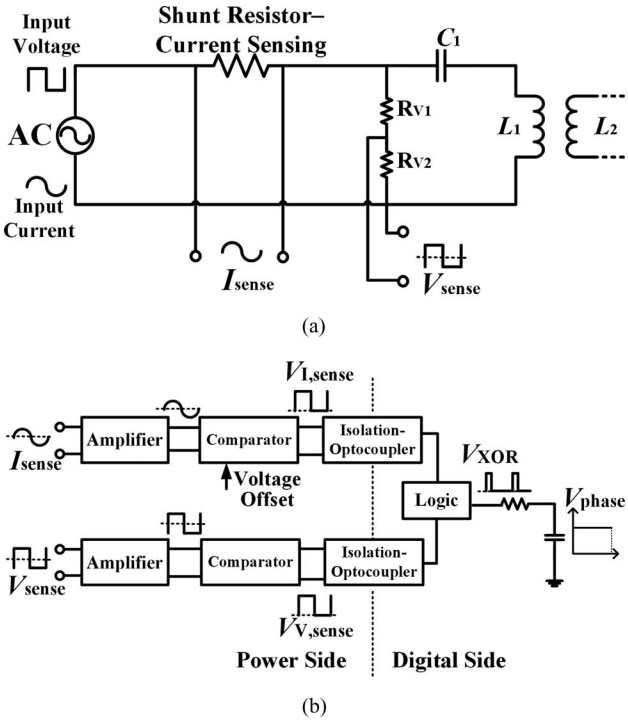

Fig. 5. (a) Schematic of sensing the input voltage and current and (b) schematic of the control loop for measuring the load-phase angle.

each step of frequency variance should be of a small value; and, the interval between every two steps should be long enough for the system to reach stability.

The control-loop can determine the *LC* connection in the load by a similar method, without using wireless communication between the charger and EVs. When the frequency is the resonant frequency f_0, the load-phase angle θ of the system with an S-connected *LC* in the load is different from the system with a P-connected *LC* in the load. The angle θ is zero at f_0 when the load contains an S-connected *LC* circuit, while θ is apparently lower than zero when the load contains a P-connected *LC* circuit. If the series connection of the *LC* circuit in the load is detected, the UIC can further adjust the frequency during the charging process to realize higher efficiency and better charging quality. From the curves of load-phase angle of the SS topology, the power factor (P/S, where P is the real power and S is the apparent power of the system) of the system reduces when the equivalent resistance *R* increases. Accordingly, the UIC can reduce the frequency to a lower value than f_1, as

$$f = f_0 + (f_1 - f_0)/\eta \quad (\eta > 1) \tag{10}$$

when the load-phase angle is large enough (the load becomes light enough). Then, the power factor is increased and the power loss generated by parasitic resistors is reduced. Because of the limitations on the input voltage of the on-board dc–dc converter and the standard of the ac frequency, the reduced ac frequency should have a lowest boundary.

B. Hardware Requirements

To realize the frequency control, the system should acquire at least the phase angle between the input voltage and current. The Hall-effect or other sensors are normally used to detect the voltage and current. However, the standard ac frequency is higher than 80 kHz, which is too high for common Hall-effect sensors to catch up with the signal in the resonant circuits. Hence, the proposed control loop captures the input voltage and current by shunt resistors and applies logic circuits to transfer the phase angle to a constant voltage output, as shown in Fig. 5. The way to sense the input voltage and current is shown in Fig. 5(a). The sensed voltage signal $V_{\rm sense}$ is acquired by resistive voltage ratio and the sensed current $I_{\rm sense}$ is got by the voltage of the shunt resistor. The specific structure of the control loop for tracking the fixed-gain point, or f_1, is shown in Fig. 5(b). First, an amplifier and a comparator are used to transfer the sensed voltage or current ($V_{\rm sense}$ or $I_{\rm sense}$) to a square wave ($V_{\rm V,sense}$ or $V_{\rm I,sense}$) with the same frequency and the same zero-crossing point. Second, let the square waves $V_{\rm V,sense}$ and $V_{\rm I,sense}$ go through a logic circuit. The logic circuit generates another square wave $V_{\rm XOR}$ with the width equal to the delay between the $V_{\rm V,sense}$ and $V_{\rm I,sense}$. Third, the *RC* circuit at the output of the logic circuit transfers $V_{\rm XOR}$ to an average voltage $V_{\rm phase}$, which is proportional to the phase angle. At last, the digital signal processor (DSP) calculates the phase angle by measuring $V_{\rm phase}$. According to the speed limitation of common ADC models, the proposed control loop is much more practical. It does not need fast measurement to get a certain amount of the voltage or current points in a period [34]; the varied frequency has no influence on the result; there is no mandatory rule on the specific measuring moments.

For more accurate measurement, a voltage offset is placed on the comparator in the branch of $I_{\rm sense}$. The voltage offset is used to counteract the phase shift caused by the parasitic inductances or capacitances of resistors around the amplifiers, as the phase-shift leads to inaccuracy of $V_{\rm XOR}$. To determine the specific offset, let the input voltage and current be in the same

phase with a standard frequency; then adjust the voltage offset to be a certain value until the detected phase-difference V_{XOR} is zero. The error caused by the unwanted phase shift can also be rectified in the DSP by adjusting the relevant codes.

C. Frequency Control in Extreme Cases

For a more comprehensive control strategy, it is necessary to consider the situation that the mutual inductance between coils is of an extreme high or low value. In previous analysis, the frequency f_1 at the fixed-gain point is determined by the mutual inductance, as indicated by (6) and (9). A larger mutual inductance *M* leads to a higher f_1. Hence, the calculated frequency f_1 may be out of the standard range of the ac frequency, when the mutual inductance between coils is extremely high or low. For example, in the simulation results shown in Fig. 2(a), the theoretical value of f_1 can be out of the SAE standard of frequency range: 81.38 kHz $\sim$ 90 kHz, when the mutual inductance *M* is lower than 10 μH or higher than 57 μH ($M = 21 \sim 55$ μH when the air-gap ranging from 20 to 10 cm). As a result, if the optimal frequency f_1 is out of the standard range, the frequency will be forcibly set as the boundary values 90 kHz (*M* is too high) or 81.5 kHz (*M* is too low). Similar to the voltage gain after varying the frequency during the charging process, the voltage gain is not fixed when the frequency is set to be the boundary values. But, compared with other frequencies, the boundary values are still the best choices in the extreme cases, because the variance of the voltage gain through the charging process is much smaller than the voltage-gain variance when the frequency is of other values.

D. Frequency Control with Nonideal LC

The simulations in Fig. 2 are based on the fact that the resonant frequency of the primary *LC* is the same as the resonant frequency of the secondary *LC*. However, it is possible that the resonant components in *LC* circuits are not ideal, because of components aging or the influence from metallic objects in the surrounding space, such as vehicle chassis. The nonideal devices may move the range of the practical f_1 to a lower or higher section, when the range of varied *M* is fixed. For example, when the secondary capacitance in the simulation of Fig. 2(a) increases from 20.7 to 21.7 nF, the resonant frequency of the secondary *LC* is varied from 78 to 76.2 kHz. The nonideal curves of the dc characteristics are shown in Fig. 6. The fix-gain point is moved to a lower value by 0.2 kHz and there is a small variance of the voltage gain the fixed-gain point. The load-phase angle at the ideal resonant frequency is not fixed at 0, as the part surrounded by the red circle. But there is still one zero-crossing point higher than f_0 for each load-phase-angle curve, meaning the control method works well. It is also possible that there are two zero-crossing points beyond the ideal f_0 on a single load-phase-angle curve. Then, the system needs to measure the load-phase angle by a certain amount of times beyond the first tracked zero-crossing point, until the highest zero-crossing point is found. As the fixed-gain point locates right beyond the highest zero-crossing point of the load-phase angle, the fixed-gain point can be still determined by the proposed method.

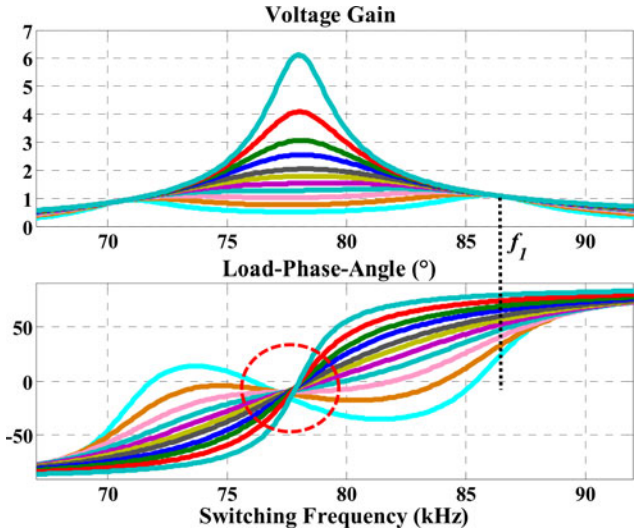

Fig. 6. Simulated dc characteristics: the voltage gain and load-phase angle versus the AC frequency in the SS-connected *LC*, where $L_1 = 199.5$ μH and $L_2 = 200.8$ μH, $C_1 = 20.9$ nF and nonideal $C_2 = 21.7$ nF, $M = 40$ μH, and $R = 10$, 15, 20, 25, 30, 35, 40, 50, 60, 80, 120 Ω.

E. Application of LLC Topology

Under the circumstances with strict limitations on the ac frequency (the SAE standard) or requiring a relatively fixed working frequency, an additional inductor can be added in the primary *LC* circuit to reduce the influence of the air-gap or coil misalignment on f_1. As indicated by (6) and (9), the influence of *M* on f_1 is reduced if the value of L_1 increases. For example, if the added inductor is

$$L_1' = \alpha L_1 \tag{11}$$

a larger α leads to a smaller range of f_1, considering all possible values of *M*. With a high enough α, the optimal frequency f_1 can be nearly constant in most of possible charging conditions. However, offsets exist when choosing α, such as the reduced power-transfer capability and the efficiency. With an additional inductor, the resonant frequency of the primary *LC* circuit should be the same: the primary resonant capacitance C_1 should be adjusted accordingly, as the new L_1 is the sum of the inductance of the transmitting coil and added inductance L_1'. The voltage gain of an S-connected load with an additional inductor is reduced to

$$G = \sqrt{L_2/(L_1 + L_1')}. \tag{12}$$

Meanwhile, the power factor with light loads becomes lower. The voltage stress on the primary resonant capacitors is increased, meaning that the charger needs capacitors with higher voltage tolerance.

IV. Design of Charging Interfaces

In an IPT system, a better charging pad generates better coupling, with the same air gap and horizontal misalignment. To the best of our knowledge, two types of pads are most commonly used in the inductive charging: the nonpolarized pads,

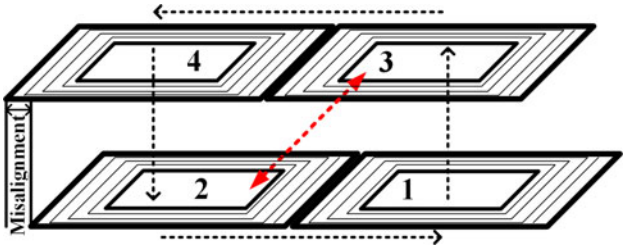

Fig. 7. Paths of magnetic flux generated by polarized pads: the black dash lines represent normal flux and the red line represents the unwanted coupling.

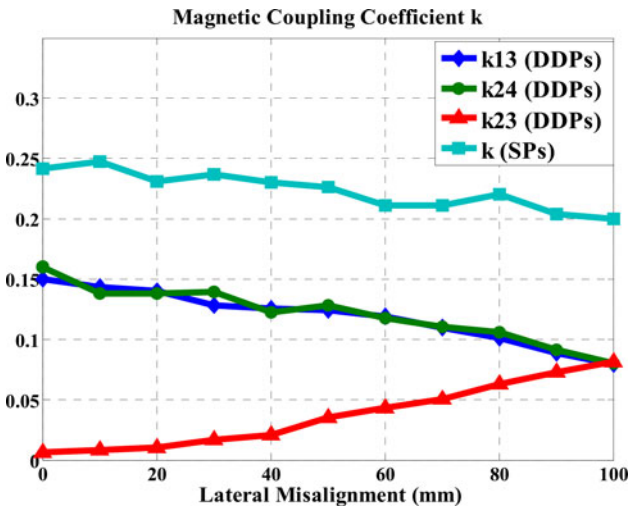

Fig. 8. Simulated coupling coefficients between coils 1 and 3 (k_{13}), 2 and 4 (k_{24}), and 2 and 3 (k_{23}) of the DDPs in Fig. 7, comparing to the coupling coefficient (k) between the coils of SPs, with the same air gap 12 cm, and various lateral misalignment $0 \sim 100$ mm.

such as circular pads (CP) or square-shaped pads (SP), and polarized pads such as bipolar pads (BPP), Double-D or Double-D Quadrature pads (DDQP) [1], [22], [28], [35], [36].

Polarized pads have been proved to have higher tolerance to the horizontal misalignment, because of the horizontally directed (parallel) flux on the surface of the pads. For example, a BPP is capable of normally operating with a polarized pad, and provides perpendicular flux when another coil is nonpolarized. For a more developed pad DDQP, the Q-coil can be used for coupling with the receiving pad when horizontal displacement reaches to a certain point (no net flux through DD coils) [28]. To operate the charger with a BPP or DDQP, it is commonly necessary to install location- or flux sensors and apply complicate control on the currents in different coils. Moreover, for a typical polarized pad, the higher tolerance of misalignment only exists in the lateral direction. This strongly limits the advantage of bipolar pads. In the contrast, a nonpolarized pad has the same tolerance of misalignment in each direction and is easy to operate. In the aspect of coupling effect, with an equal overall size, the size of the one coil in a polarized pad is smaller than the only coil of a nonpolarized pad, leading to a lower magnetic coupling coefficient ($k = M/\sqrt{L_1 L_2}$) [28], [35], [37]. This is a very important advantage of nonpolarized pad, because the size of charging pads is usually limited in practical applications. More seriously, the flux in one coil of the receiving polarized pad is seriously influenced when the wrong coil (with inverse polar) of the transmitting pad moved to partly face this receiving coil, as shown in Fig. 7. Magnetic simulations in Fig. 8 are used to prove the advantages of nonpolarized pads. In Fig. 8, the DDPs and SPs have the same overall size (40 cm $\times$ 40 cm), the same number of coil turns (20 turns by two-parallel-connected wires), and the same air gap between the transmitting and receiving pads. In the simulations, the reasonable coupling coefficients k_{13} and k_{24} of the DDP–DDP pair (in Fig. 7) are lower than the coupling coefficient k between the SPs. Meanwhile, the unwanted coupling coefficient k_{23} between the coil 2 and 3 is increased by the lateral misalignment, which seriously influences the overall coupling effect. The BPPs have similar trends of the magnetic coupling. Obviously, with limitations on the pad size, a SP performs much better. The popularity of the nonpolarized pad in the current research is also an advantage for its practical application. As a result, the nonpolarized pad is chosen as the charging interface for the proposed UIC.

In practical applications, the size limitation on the charging pads is commonly on the diameter (CP), the side-length (SP) or width and length (rectangular pad) of the coil. This means that the maximum coupling coefficient can be realized by SPs with the longest edges, because the area of a SP is significantly higher than a CP when the edge of the SP is equal to the diameter of the CP [28]. The selection of the specific shape of charging pads also depends on the parameter M^2/L_2, which determines the power capability of the system [12]. Magnetic simulations are built on SPs and CPs with the same length of the outer and inner length or diameter: the SP with the inner edge of 28 cm, the outer edge of 40 cm and 20 turns two-parallel-connected wires, and the CP with the inner diameter of 28 cm, the outer diameter of 40 cm and 20 turns two-parallel-connected wires. By comparing the value of M^2/L_2 with combinations of CP&CP, CP&SP, SP&SP, in various air gap and misalignment, a pair of square-shaped pads has the highest M^2/L_2, as shown in Fig. 9. The curves for the coupling coefficient of the three combinations are in the similar trend. So, a square-shaped pad is the optimal design of the universal charging pad in the proposed system. In practical applications, the specific size of a SP can be chosen according to the size limitation by EV manufacturers.

For the specific parameter of the charging interface, such as the number of the coil turns, dimensions, and the application of ferrite bars, they are also determined by the planned voltage and current of the IPT system. The first matter coming to mind is the voltage gain, which is determined by the self-inductances of the coils, according to (5) and (8). Moreover, with the same current level, a coil with larger self-inductance generates a higher voltage stress on the resonant capacitor, which has a certain limitation. In some applications, the coil-wires are parallel connected, to reduce the self-inductance.

V. Experimental Results

A 5-kW (maximum power) prototype has been built to test the applicability of the proposed system, shown in Fig. 10. The prototypes of the transmitting and receiving coils are shown in

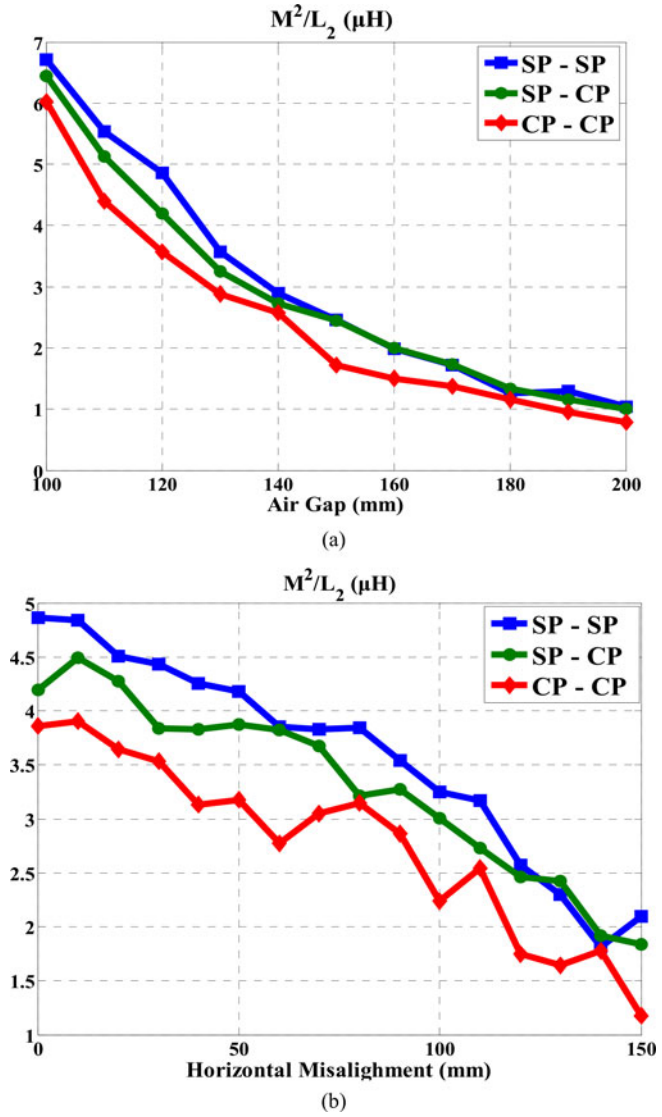

Fig. 9. Simulated parameter M^2/L_2 versus (a) air gap (100 $\sim$ 200 mm, 0 horizontal misalignment), and (b) horizontal misalignment (0 $\sim$ 150 mm, 120 mm air gap), with three different pad combinations.

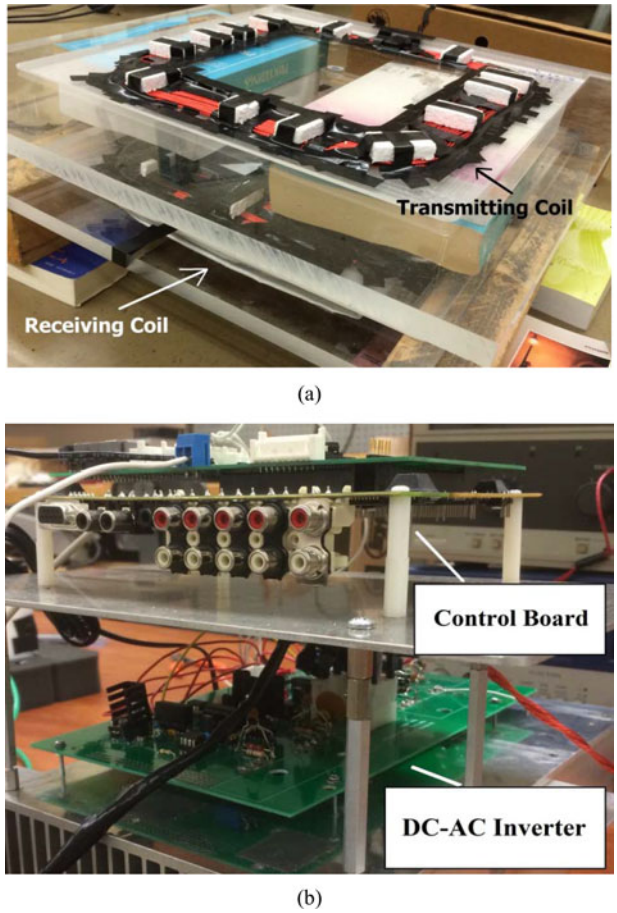

Fig. 10. Prototype, including (a) transmitting and receiving coils; (b) dc–ac inverter and the control board.

TABLE I
PARAMETERS OF TRANSMITTING AND RECEIVING COILS

Parameter	Trans coil	Recei Coil 1	Recei Coil 2
Dimensions	Inner length 28 cm, Outer length 40 cm.	Inner length 28 cm, Outer length 40 cm.	Inner diameter 20 cm, Outer diameter 28 cm.
Inductance	199.5 μH	200.8 μH	89.8 μH
Resonant Capacitance	20.9 nF	20.7 nF	46.6 nF
Turn NO.	20	20	15
Threads/Turn	2	2	1
Others		Four Ferrite-Bars on Back	Four Ferrite-Bars on Back

Fig. 10(a). Two types of receiving coils, an SP (Coil 1) and a CP (Coil 2) are used for testing. The parameters of each coil and resonant capacitance are listed in Table I. Note that the SPs in the hardware are the same as those used in magnetic simulations. The primary dc–ac inverter is a full-bridge inverter built by four MOSFETs, FDH44N50 (500 V, 44 A), shown in Fig. 10(b). A control loop is built based on DSP and FPGA. The DSP focuses on switch-signal calculations and FPGA does voltage and current measurement and generating gate-drive signals. A control model made by analog devices and logic circuits is used to detect f_1, based on the structure in Fig. 5.

A. Experimental Results With Receiving Coil 1

When the receiving coil is the coil 1, the efficiency and the voltage gain *G* versus the frequency are measured, with various values of the air gap, as shown in Fig. 11. The selection of the frequency with different air gaps is realized by the control model proposed in Section III. The ZVS is realized by the system in all four coupling conditions. The control model selects the optimal frequency with the lowest *R* (full load) and keeps the frequency constant during the charging process. According to the curves of the efficiency and the voltage gain, the following results are acquired:

1) the optimal frequency f_1 acquired becomes lower when the mutual coupling is reduced;

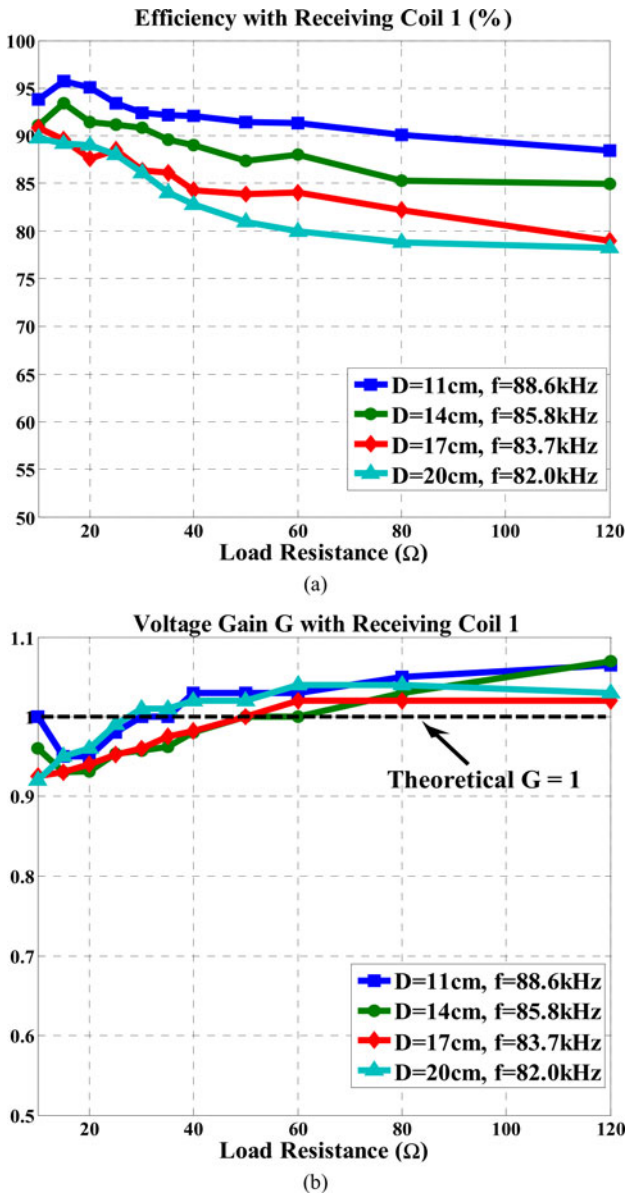

Fig. 11. (a) System efficiency and (b) voltage gain versus $R(= 10, 15, 20, 25, 30, 35, 40, 50, 60, 80, 120\ \Omega)$, with different air-gaps D, when the load contains the coil 1.

2) the efficiency of the system reduces when the air gap increases;
3) with a fixed frequency during the charging process, the efficiency of the system generally reduces as R increases (the load becomes light);
4) the voltage gain is kept around the theoretical value $G = 1$, but the specific trend of each curve depends on the value of the air gap.

By analysis, the larger the mutual inductance is, the more influence the secondary side has on the primary side, as the relatively larger impedance is reflected to the primary side. As a result, the fixed-gain point will be shifted to be a larger value from the resonant frequency when the mutual coupling increases. This phenomenon is also demonstrated by simulations in Fig. 2.

As shown in Fig. 2, the phase-angle increases (>0) and the power factor reduces, when the frequency is kept constant at the fixed-gain point and R increases. The efficiency reduces when the power factor of the whole system is reduced, because more power is consumed by the parasitic resistance. However, when the air gap is 11 or 14 cm, the efficiency first increases, and then, reduces. The main reason for this trend is the higher current level with heavier loads. With a heavy load, the power loss by uncoupling flux or environmental impacts is more apparent and occupies the main part of the loss. In the circuit model, there is an equivalent resistance r' connected with M (shown in Fig. 1), simulating the power consumption caused by flux leakage or unwanted coupling. When the coupling reduces, the power consumed by r' becomes relatively stable during charging, and the power loss caused by resonant components becomes the main reason of the efficiency variance. In other words, when the coupling between the coils is tighter, the influence of the current level (influenced by load variance) is more serious. This analysis can also be applied to the variance of the voltage gain. With tighter coupling (11 and 14 cm air gaps), G first decreases, and then, increases, as R increases. For the voltage-gain curves of $D = 17$ cm and $D = 20$ cm, G increases as the load becomes light. Although the voltage gain is not strictly kept as the ideal value, it is still much more reasonable for G to be maintained in a range from 0.92 to 1.07, than the range from 0.3 to 6 with the resonant frequency. In fact, another reason for the inaccurate output is that the frequency set by the system is not exactly the theoretical f_1. The theoretical f_1 should be got by the zero phase angle with an extremely small R. The practical f_1 is acquired at the heaviest load, meaning that the frequency is a bit lower than f_1, although the ZVS can be realized. So there is a small error between the working frequency and the fixed-gain frequency.

B. Experimental Results With Receiving Coil 2

With the receiving coil 2, the system efficiency and the voltage gain are shown in Fig. 12. Still, a larger air gap leads to a lower optimal frequency; with a fixed air gap, the efficiency keeps reducing as the load becomes light. Here, the variances of the system efficiency and the voltage gain versus D or R are similar to the curves of $D = 17$ cm and $D = 20$ cm in Fig. 11, for relatively loose coupling.

Obviously, the efficiency with the coil 2 is lower than the efficiency with the coil 1. The main reason for the lower efficiency is the looser coupling between the transmitting and receiving coils. As the receiving coil 2 is much smaller than the transmitting coil, more flux leakage is generated. This is also the reason why a square-shaped coil is preferred, for its larger charging area with better coupling [35]. By magnetic simulations, a reasonable combination of the charging interfaces requires two coils to have similar sizes.

C. Variable-Frequency Control

The variable-frequency control is applied in the hardware experiments, with the receiving coil 1. Based on (10), the phase-angle threshold for frequency variance is set to be 40 degrees

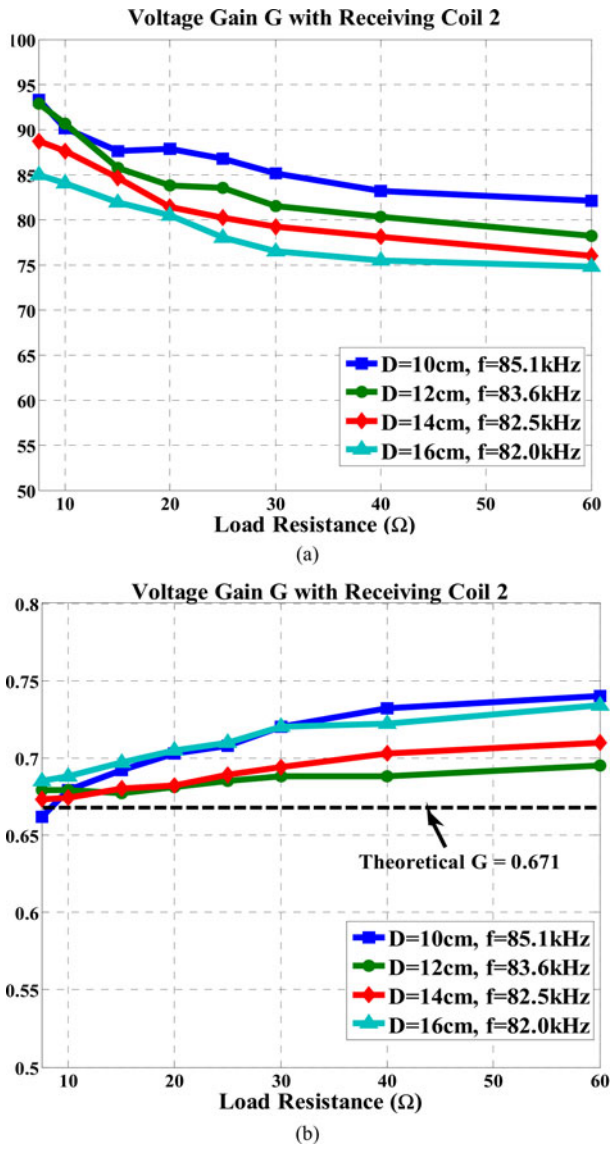

Fig. 12. (a) System efficiency and (b) voltage gain versus $R(= 7.5, 10, 15, 20, 25, 30, 40, 60\ \Omega)$, with different air-gaps D, when the load contains the coil 2.

and the coefficient of frequency variance η is 1/5. Then, the experiment results are as follows:

1) $D = 11$ cm, the frequency is adjusted from 88.6 to be 87.2 kHz, when $R = 30\ \Omega$;
2) $D = 14$ cm, the frequency is adjusted from 85.5 to be 84.6 kHz, when $R = 25\ \Omega$;
3) $D = 17$ cm, the frequency is adjusted from 83.7 kHz to be 83.3 kHz, when $R = 20\ \Omega$;
4) $D = 20$ cm, the frequency is kept as 82.0 kHz, because the lowest bound for the frequency is 81.8 kHz.

Note that the variance of frequency is realized by multiple small steps, as $0.1 \sim 0.16$ kHz for each step in these experiments. And, the interval between each two steps is 10 s.

D. Accuracy of Tracked f_1

As mentioned in Part A, there is a small error between the theoretical f_1 and the practical f_1 acquired by the proposed control method, leading to a nonconstant charging voltage $V_{\rm out}$ during the charging process, as shown in Figs. 11(b) and 12(b). Based on the various coupling effects in Figs. 11 and 12, comparisons have been made between practical f_1 acquired in experiments and the theoretical values, as shown Fig. 13. The theoretical values are accurately measured by the oscilloscope and the voltage-gain analysis. In Fig. 13, the theoretical value of f_1 is consistently higher than the acquired value. The error ranges from 0.3 to 0.8 kHz, with relatively larger values in better coupling (smaller air gap). The main reason for the error is from the equivalent resistance R. In fact, the practical f_1 is tracked when the load is the heaviest R; but, the theoretical value of f_1 should be tracked with the extremely small R. The error is acceptable, because the variance of the voltage gain is very limited.

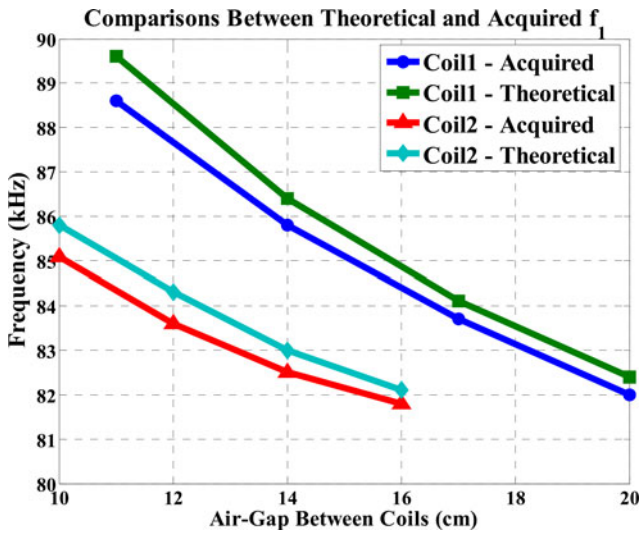

Fig. 13. Theoretical values of f_1 and acquired values of f_1 by the proposed control method, with coil 1 and 2, in various coupling conditions (air gaps).

E. ZVS of the Primary DC–AC Inverter

Based on the proposed frequency control, ZVS (turn-on) has been universally realized in all charging conditions with the coil 1 and 2. For example, a set of waveforms for typical ZVS operation is shown in Fig. 14. In Fig. 14, it is obvious that the equivalent load for the primary dc–ac inverter is inductive, as the input current of the primary *LC* circuits lags the input voltage. During Δt, the current flows through the body diode of the measured MOSFET, which has not been turned ON yet. The drain-to-source voltage $V_{\rm DS}$ of the MOSFET is kept nearly zero at the moment. After Δt, the gate-driving signal turns ON the MOSFET with zero $V_{\rm DS}$ and ZVS is realized. As a result, an inductive equivalent load leads to ZVS-ON of the dc–ac inverter in the primary side. According to the load-phase-angle curves in Fig. 2, the phase difference between the input voltage and current is increased when the load becomes light. This means that if the heaviest load is inductive (ZVS), the equivalent load will be kept inductive during the whole charging process. As the frequency can be adjusted with various coupling effects, ZVS can be universally realized in every charging cycle.

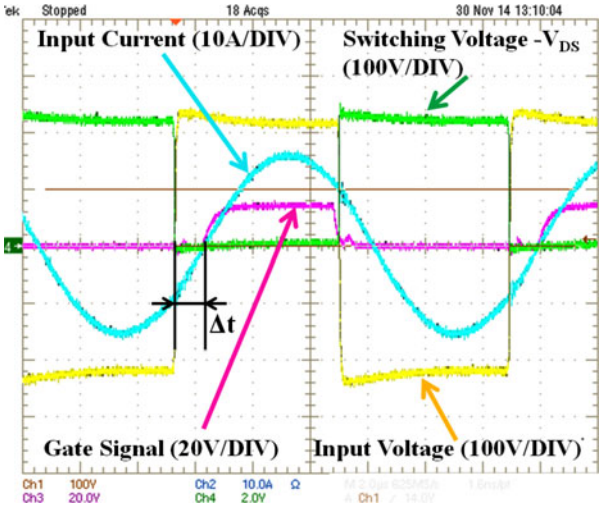

Fig. 14. Input voltage and current of the primary *LC* circuit, and the gate-driving signal and drain-to-source Voltage V_{DS} of the relevant MOSFET (as Q_1 in Fig. 3), when the load contains the coil 1, $D = 14$ cm, $R = 30\ \Omega$, the input dc voltage $= 200$ V, and the frequency $= 85.8$ kHz.

VI. Conclusion

A UIC is proposed to provide the stable and controllable charging voltage to loads with different characteristics via varied magnetic coupling between the charging coils. A specific standard of the UIC for EVs is proposed in this paper. The S-connected *LC* circuit is proved to be the optimal topology for primary resonant circuit. A control method is applied to select the optimal frequency, based on the load-phase angle. A nonpolarized coil in square shape is preferred as the charging interface. Hardware experiments have demonstrated the high efficiency and universality of the proposed system, with the following advantages.

1) *Universal Application:* Facing with the market with more and more EV models, the proposed system can provide stable and controllable charging voltage to various EVs with different receiving coils, connections of *LC* circuits, load ranges, etc.
2) *Adaptive Frequency Control:* with a wide range of the varied mutual inductance, the proposed system can provide stable charging voltage by adjusting the ac frequency to be an optimal value automatically. Moreover, the ac frequency can be further adjusted during the charging process to increase the power factor and efficiency.
3) *Effective V&I Sensing:* The proposed control loop has no requirement on the speed of sensing and A/D conversion. It is also capable of detecting the *LC* connection.
4) *High Efficiency:* in the proposed system, the ZVS is kept during the charging process, leading to lower power loss. With the same air gap and misalignment between coils, the square-shaped coil generates tighter coupling and less leakage flux, meaning less power losses.

References

[1] L. Nan and T. G. Habetler, "A study of designing a universal inductive charger for Electric Vehicles," in *Proc. IEEE 39th Annu. Ind. Electron. Soc. Conf.*, 2013, pp. 4528–4533.
[2] H. H. Wu, A. Gilchrist, K. Sealy, and D. Bronson, "A 90 percent efficient 5 kW inductive charger for EVs," in *Proc. IEEE Energy Convers. Congr. Expo.*, 2012, pp. 275–282.
[3] N. Liu and T. G. Habetler, "Design of a universal inductive charger for electric vehicles," in *Proc. IEEE Transp. Electrification Conf. Expo.*, 2014, pp. 1–6.
[4] W. Chwei-Sen, O. H. Stielau, and G. A. Covic, "Design considerations for a contactless electric vehicle battery charger," *IEEE Trans. Ind. Electron.*, vol. 52, no. 5, pp. 1308–1314, Oct. 2005.
[5] M. G. Egan, D. L. O'Sullivan, J. G. Hayes, M. J. Willers, and C. P. Henze, "Power-factor-corrected single-stage inductive charger for electric vehicle batteries," *IEEE Trans. Ind. Electron.*, vol. 54, no. 2, pp. 1217–1226, Apr. 2007.
[6] J. Sallan, J. L. Villa, A. Llombart, and J. F. Sanz, "Optimal design of ICPT systems applied to electric vehicle battery charge," *IEEE Trans. Ind. Electron.*, vol. 56, no. 6, pp. 2140–2149, Jun. 2009.
[7] S. Krishnan, S. Bhuyan, V. P. Kumar, W. Wenjiang, J. A. Afif, and L. Khoon Seong, "Frequency agile resonance-based wireless charging system for Electric Vehicles," in *Proc. IEEE Int. Electric Vehicle Conf.*, 2012, pp. 1–4.
[8] J. G. Hayes, M. G. Egan, J. M. D. Murphy, S. E. Schulz, and J. T. Hall, "Wide-load-range resonant converter supplying the SAE J-1773 electric vehicle inductive charging interface," *IEEE Trans. Ind. Appl.*, vol. 35, no. 4, pp. 884–895, Jul./Aug. 1999.
[9] L. Kibok, Z. Pantic, and S. M. Lukic, "Reflexive field containment in dynamic inductive power transfer systems," *IEEE Trans. Power Electron.*, vol. 29, no. 9, pp. 4592–4602, Sep. 2014.
[10] Z. Wei, W. Siu-Chung, C. K. Tse, and C. Qianhong, "Design for efficiency optimization and voltage controllability of series-series compensated inductive power transfer systems," *IEEE Trans. Power Electron.*, vol. 29, no. 1, pp. 191–200, Jan. 2014.
[11] E. Waffenschmidt and T. Staring, "Limitation of inductive power transfer for consumer applications," in *Proc. 13th Eur. Conf. Power Electron. Appl.*, 2009, pp. 1–10.
[12] J. T. Boys, G. A. Covic, and A. W. Green, "Stability and control of inductively coupled power transfer systems," *IEE Proc. - Electric Power Appl.*, vol. 147, no. 1, pp. 37–43, Jan. 2000.
[13] D. O'Sullivan, M. Willers, M. G. Egan, J. G. Hayes, P. T. Nguyen, and C. P. Henze, "Power-factor-corrected single-stage inductive charger for electric-vehicle batteries," in *Proc. IEEE 31st Annu. Power Electron. Spec. Conf.*, 2000, vol. 1, pp. 509–516.
[14] L. Yongseok, T. Hoyoung, L. Seungok, and P. Jongsun, "An adaptive impedance-matching network based on a novel capacitor matrix for wireless power transfer," *IEEE Trans. Power Electron.*, vol. 29, no. 8, pp. 4403–4413, Aug. 2014.
[15] Z. Pantic, B. Sanzhong, and S. Lukic, "ZCS LCC-compensated resonant inverter for inductive-power-transfer application," *IEEE Trans. Ind. Electron.*, vol. 58, no. 8, pp. 3500–3510, Aug. 2011.
[16] Z. Cong, C. Rui, E. Faraci, Z. U. Zahid, M. Senesky, D. Anderson, J.-S. Lai, Y. Wensong, and C.-Y. Lin, "High efficiency contactless power transfer system for electric vehicle battery charging," in *Proc. IEEE Energy Convers. Congr. Expo.*, 2013, pp. 3243–3249.
[17] C. Rui, Z. Cong, Z. U. Zahid, E. Faraci, Y. Wengsong, L. Jih-Sheng, M. Senesky, and D. Anderson, "Analysis and parameters optimization of a contactless IPT system for EV charger," in *Proc. IEEE 29th Annu. Appl. Power Electron. Conf. Expo.*, 2014, pp. 1654–1661.
[18] I. Nam, R. Dougal, and E. Santi, "Novel control approach to achieving efficient wireless battery charging for portable electronic devices," in *Proc. IEEE Energy Convers. Congr. Expo.*, 2012, pp. 2482–2491.
[19] D. J. Thrimawithana, U. K. Madawala, and M. Neath, "A synchronization technique for bidirectional IPT systems," *IEEE Trans. Ind. Electron.*, vol. 60, no. 1, pp. 301–309, Jan. 2013.
[20] S. Aldhaher, P. C. K. Luk, and J. F. Whidborne, "Electronic tuning of misaligned coils in wireless power transfer systems," *IEEE Trans. Power Electron.*, vol. 29, no. 11, pp. 5975–5982, Nov. 2014.
[21] M. Budhia, J. T. Boys, G. A. Covic, and H. Chang-Yu, "Development of a single-sided flux magnetic coupler for electric vehicle IPT charging systems," *IEEE Trans. Ind. Electron.*, vol. 60, no. 1, pp. 318–328, Jan. 2013.
[22] G. A. Covic, M. L. G. Kissin, D. Kacprzak, N. Clausen, and H. Hao, "A bipolar primary pad topology for EV stationary charging and highway power by inductive coupling," in *Proc. IEEE Energy Convers. Congr. Expo.*, 2011, pp. 1832–1838.
[23] Z. Pantic, K. Lee, and S. Lukic, "Inductive power transfer by means of multiple frequencies in the magnetic link," in *Proc. IEEE Energy Convers. Congr. Expo.*, 2013, pp. 2912–2919.

[24] S. Y. R. Hui and W. W. C. Ho, "A new generation of universal contactless battery charging platform for portable consumer electronic equipment," *IEEE Trans. Power Electron.*, vol. 20, no. 3, pp. 620–627, May 2005.
[25] L. Sungwoo, H. Jin, P. Changbyung, C. Nam-Sup, C. Gyu-Hyeoung, and R. Chun-Taek, "On-line electric vehicle using inductive power transfer system," in *Proc. IEEE Energy Convers. Congr. Expo.*, 2010, pp. 1598–1601.
[26] C. Kainan and Z. Zhengming, "Analysis of the double-layer printed spiral coil for wireless power transfer," *IEEE J. Emerg. Sel. Topics Power Electron.*, vol. 1, no. 2, pp. 114–121, Jun. 2013.
[27] A. Zaheer, D. Kacprzak, and G. A. Covic, "A bipolar receiver pad in a lumped IPT system for electric vehicle charging applications," in *Proc. IEEE Energy Convers. Congr. Expo.*, 2012, pp. 283–290.
[28] R. Bosshard, J. W. Kolar, J. Muehlethaler, I. Stevanovic, B. Wunsch, and F. Canales, "Modeling and η-α-Pareto optimization of inductive power transfer coils for electric vehicles," *IEEE J. Emerg. Sel. Topics Power Electron.*, to be published.
[29] O. H. Stielau and G. A. Covic, "Design of loosely coupled inductive power transfer systems," in *Proc. Int. Conf. Power Syst. Technol.*, 2000, vol. 1, pp. 85–90.
[30] M. Yilmaz and P. T. Krein, "Review of battery charger topologies, charging power levels, and infrastructure for plug-in electric and hybrid vehicles," *IEEE Trans. Power Electron.*, vol. 28, no. 5, pp. 2151–2169, May 2013.
[31] G. A. Covic, J. T. Boys, A. M. W. Tam, and J. C. H. Peng, "Self tuning pick-ups for inductive power transfer," in *Proc. IEEE Power Electron. Spec. Conf.*, 2008, pp. 3489–3494.
[32] H. Ishihara, F. Moritsuka, H. Kudo, S. Obayashi, T. Itakura, A. Matsushita, H. Mochikawa, and S. Otaka, "A voltage ratio-based efficiency control method for 3 kW wireless power transmission," in *Proc. IEEE Appl. Power Electron. Conf. Expo.*, 2014, pp. 1312–1316.
[33] L. Nan and W. Bingnan, "An LLC-based planar wireless power transfer system for multiple devices," in *Proc. IEEE 29th Annu. Appl. Power Electron. Conf. Expo.*, 2014, pp. 3411–3417.
[34] N. S. Bayindir, O. Kukrer, and M. Yakup, "DSP-based PLL-controlled 50–100 kHz 20 kW high-frequency induction heating system for surface hardening and welding applications," *Proc. IEE*, vol. 150, no. 3, pp. 365–371, May 2003.
[35] H. M. Greenhouse, "Design of planar rectangular microelectronic inductors," *IEEE Trans. Parts, Hybrids, Packag.*, vol. PHP-10, no. 2, pp. 101–109, Jun. 1974.
[36] A. Zaheer, H. Hao, G. A. Covic, and D. Kacprzak, "Investigation of multiple decoupled coil primary pad topologies in lumped IPT systems for interoperable electric vehicle charging," *IEEE Trans. Power Electron.*, vol. 30, no. 4, pp. 1937–1955, Apr. 2015.
[37] S. Raju, W. Rongxiang, C. Mansun, and C. P. Yue, "Modeling of mutual coupling between planar inductors in wireless power applications," *IEEE Trans. Power Electron.*, vol. 29, no. 1, pp. 481–490, Jan. 2014.

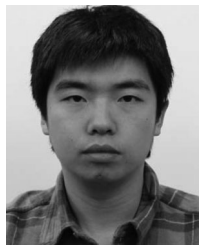

Nan Liu (S'12) received the B.S. degree in electrical engineering from Zhejiang University, Hangzhou, China, in 2011. He is currently working toward the Ph.D. degree at the School of Electrical and Computer Engineering, Georgia Institute of Technology, Atlanta, GA, USA.

His research interests include inductive power transfer and resonant converters.

Thomas G. Habetler (S'82–M'83–S'85–M'89–SM'92–F'02) received the B.S.E.E. degree, in 1981, and the M.S. degree, in 1984, both in electrical engineering, from Marquette University, Milwaukee, WI, USA, and the Ph.D. degree from the University of Wisconsin-Madison, Madison, WI, in 1989.

Since 1989, he has been with the Georgia Institute of Technology, Atlanta, GA, USA, where he is currently a Professor of electrical engineering. His research interests include electric machine protection and condition monitoring, and drives, and has published more than 300 papers in the field. He is a regular Consultant to industry in the field of condition-based diagnostics for electrical systems.

Dr. Habetler received the Power Electronics Society Diagnostics Achievement Award, the Harry A. Owen Distinguished Service Award, the IAS Gerald Kliman Innovator Award, and the EPE-PEMC Outstanding Achievement Award. He also received five conference prize paper awards and a transactions paper award from the Industry Applications Society. He has served on the IEEE Board of Directors as Division II Director from 2007 to 2008, is a Past President of the IEEE Power Electronics Society, and has served on the IEEE Member and Geographic Activities Board and on the Board of Directors of IEEE-USA.